JATIS Journal of Astronomical Telescopes, Instruments, and Systems

RESEARCH PAPER

Atomic layer deposited protective coating of aluminum oxide on silver-based telescope mirror: a comparison between a pure ozone and H_2O precursor

Søren A. Tornøe,[a,b] Brandon Cheney,[c] Brian Dupraw,[d] Yoshimasa Okamura,[e] Andrew C. Phillips,[d] Takayuki Hagiwara,[f] Tetsuya Nishiguchi,[f] and Nobuhiko P. Kobayashi[a,b,*]

[a]University of California, Santa Cruz, Baskin School of Engineering, Santa Cruz, California, United States
[b]University of California, Santa Cruz, Nanostructured Energy Conversion Technology and Research (NECTAR), Santa Cruz, California, United States
[c]University of California, Santa Cruz, Department of Earth & Planetary Sciences, Santa Cruz, California, United States
[d]University of California, Santa Cruz, University of California Observatories, Santa Cruz, California, United States
[e]Meiden America, Inc., Santa Clara, California, United States
[f]MEIDEN NANOPROCESS INNOVATIONS, Inc., Tokyo, Japan

ABSTRACT. Silver-based telescope mirrors excel in the visible infrared but require protective coatings to overcome low durability. A single-layer of aluminum oxide (AlO_x) deposited through atomic layer deposition (ALD) using trimethylaluminum and water (H_2O) at low temperatures (~60°C) protects the silver without adversely impacting the optical performance of the mirrors, but in environmental tests under high humidity at high temperatures, they degrade quickly. This paper compares the performance of AlO_x-protected silver-based mirrors using two oxygen precursors: H_2O and pure ozone (PO). Initially comparable, the reflectance of the PO-prepared samples shows a 17% improvement over those prepared with H_2O after environmental testing.

 [DOI: 10.1117/1.JATIS.10.4.044007]

Keywords: e-beam evaporation; atomic layer deposition; pure ozone; corrosion; high temperature; high humidity

Paper 24001G received Jan. 15, 2024; revised Oct. 9, 2024; accepted Oct. 11, 2024; published Nov. 4, 2024.

1 Introduction

Silver-based telescope mirrors (Ag-based mirrors) offer optical performance in the visible to infrared spectral range that excels over that of aluminum-based mirrors, though they suffer significantly from low durability in various environment tests. Our previous study has shown that a single-layer of aluminum oxide (AlO_x), with an approximate thickness of 60 nm deposited through thermal atomic layer deposition (ALD), acts as a protective coating (AlO_x protective coating) and significantly increases the working lifetime of Ag-based mirrors without negatively impacting the optical properties of the mirrors.[1–7] In designing an ALD process for any class of metal oxide, various deposition conditions such as deposition temperature, precursor pulse time, and chamber purge time are often vital for a given choice of precursors. For thermal ALD of AlO_x, H_2O is commonly used as an oxygen precursor in ALD due to its safety, ease of handling,

*Address all correspondence to Nobuhiko P. Kobayashi, nkobayas@ucsc.edu

2329-4124/2024/$28.00

and relatively simple implementation within ALD systems. However, the use of H_2O frequently requires higher deposition temperatures (100°C to 150°C) to maintain reasonable growth rates and minimize the incorporation of various contaminants,[8] presenting a significant limitation for temperature-sensitive substrates and materials. In addition, H_2O is inherently slow to desorb from the chamber, resulting in the need for longer chamber purge times after an H_2O pulse. Nevertheless, the impact of choosing a particular oxygen precursor is expected to be substantial.

This paper describes a comparative study of two types of Ag-based mirrors: one with an AlO_x protective coating deposited with a conventional oxygen precursor—water (H_2O)—and the other deposited with high-purity ozone (PO).[9] Being high purity, PO used in this study is above 80%;[9] by contrast, conventional ozone used typically contains an O_3 purity below 20%.[10] The chemical process of conventional ozone interacting with trimethylaluminum (TMA), unlike PO and TMA as used in this study, generates several intermediates that can end up as impurities in the protective oxide coating.[11] PO in turn shows a two-magnitude reduction in H_2O and NO_x impurities that consequently reduce corrosive and ion-migrated surface reactions that typically lead to increases in surface roughness.[12] Moreover, PO has the ability to effectively reduce hydrogen and methyl impurities in the films by promoting more efficient reactions with the metal precursor. A significant reduction in these hydrogen-rich impurities could potentially result in an enhanced reflectivity across the absorption spectra associated with hydrogen. The reduction of impurities yields a purer, more corrosively resistant protective oxide coating. Unlike conventional O_3, which is inherently unstable over long-term storage, the increased purity of PO, combined with the use of stainless-steel piping and fittings, significantly improves its stability throughout extended periods of operation. PO can also be used at temperatures ranging from 30°C to 60°C which is much lower than those required for H_2O. Consequently, as PO does not have the same absorption/desorption issue, chamber purge times can be significantly shortened. Compared with H_2O, the use of PO and O_3 is generally more expensive to implement, primarily due to the need for an ozone generator. The incorporation of this additional equipment increases both the operational complexity and overall cost of the deposition equipment. The goal of this study is to see how well environmentally weathered AlO_x protective coatings hold up when prepared with PO in comparison to those prepared with H_2O.

2 Materials and Methods

2.1 Sample Preparation

The Ag-based mirror sample consists of seven layers deposited on a BK7 float glass substrate as illustrated in Fig. 1. Layers 1 and 2 used ion-assisted electron-beam deposition (IAD), whereas layers 3 through 6 were deposited using physical vapor deposition (PVD) via e-beam evaporation. The IAD deposition and the e-beam deposition of layers 1 through 6 were carried out in a single PVD coating run, with a substrate temperature of 50°C. Layer 1 was a film of Y_2O_3 deposited via IAD of yttrium oxide with 36 sccm of O_2 and 16 sccm of Ar resulting in a deposition rate of 3.6 nm/s at roughly 1E−4 Torr. Layer 2 was YF_3 deposited via IAD with 20 sccm of Ar

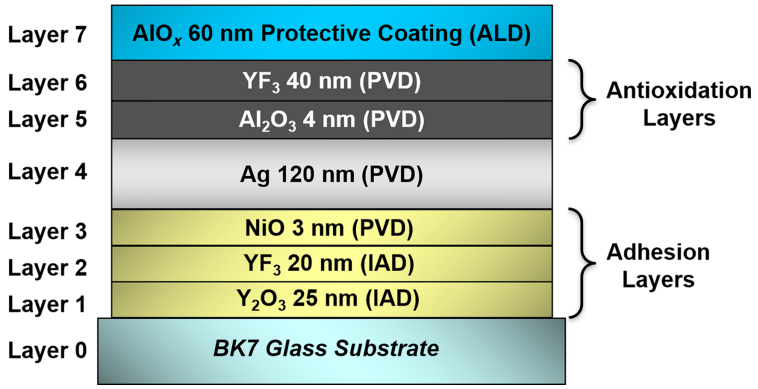

Fig. 1 General diagram representation of the samples produced for this study. With the exception of the protective coating, all layers were deposited via e-beam PVD in a single coating run.

Table 1 Information on individual depositions of layers for the mirror samples. The two processes—ALD with H_2O and PO—were independently calibrated and optimized, such that the only difference of relevance between the two types of samples is a choice of oxygen precursor.

	Material	Nominal thickness (nm)	Deposition rate [nm]	Base pressure (Torr)	Substrate temperature (°C)	Notes
Layer 7 H_2O	AlO_X	60	0.086/cycle	0.47	60	Thermal ALD with TMA and H_2O precursors, N_2 carrier gas flow: 20 sccm, 698 total cycles.
Layer 7 PO	AlO_X	60	0.160/cycle	0.15	60	Thermal ALD with TMA and PO precursors, Ar carrier gas flow: 194 sccm, 375 total cycles.
Layer 6	YF_3	40	0.60/s	8.4E−7	50	PVD, no gas flow.
Layer 5	Al_2O_3	4	0.20/s	4.2E−5	50	PVD with 25 sccm flow of O_2.
Layer 4	Ag	120	4.00/s	1.2E−6	50	PVD with Ag purity of 99.99%.
Layer 3	NiO	3	0.20/s	9.0E−5	50	PVD with 25 sccm flow of O_2.
Layer 2	YF_3	20	0.36/s	1.0E−4	50	IAD with 20 sccm of flow Ar.
Layer 1	Y_2O_3	25	0.36/s	1.0E−4	50	IAD with 36 sccm flow of O_2 and 16 sccm flow of Ar.

resulting in a deposition rate of 3.6 nm/s at roughly 1E−4 Torr. Layer 3 was a film of NiO deposited via PVD of Ni metal with a 25 sccm bleed of O_2 to form the oxide resulting in a deposition rate of 2.0 nm/s at roughly 9E−5 Torr. These adhesion layers, layers 1 through 3, are then bombarded with 10 sccm Ar and 20 sccm O_2 at 1.1E−4 Torr. This prepares the surface of the BK7 glass substrate for the deposition of layer 4—a thin film of Ag deposited at a rate of 40 nm/s at roughly 1.2E−6 Torr—to ensure that the Ag layer sticks well to the substrate. For the Ag layer, bulk properties were required, which we have defined here as the thickness of Ag required for near-zero transmittance. It has previously been determined that 80 nm of Ag has a peak transmittance of 3% at 330 nm and is near zero across the rest of the spectral range of interest.[13] As such, an Ag layer thickness of 120 nm was determined by the University of California Observatories (UCO) to optically behave such as bulk-polished Ag across the entire spectral range of interest. On top of the Ag layer, two antioxidation layers, layer 5—deposited by reactively evaporating an Al target with a 25 sccm bleed of O_2 for a deposition rate of 2.0 nm/s at roughly 4.2E−5 Torr and layer 6—YF_3 target evaporated at a rate of 6.0 nm/s at roughly 8.4E–7 Torr—were deposited to temporarily protect the surface of the Ag layer during the transfer of the samples from the PVD system to an ALD system. Layer 7 was deposited via thermal ALD at 60°C using a TMA precursor combined with either an H_2O or PO oxygen precursor, yielding two types of samples. This process, as will be shown later in the paper, was found to be highly repeatable. Further details on all the deposition processes are presented in Table 1. Between layers 1 to 6 and layer 7, as well as all subsequent points of storage, the samples were placed in individual dry boxes in a clean room environment where temperatures were kept at around $22 \pm 0.5^{\circ}$C and humidity maintained between 30% and 45%.

2.2 High-Temperature High Humidity Testing

The two types of mirror samples—one set with an AlO_x protective coating prepared with H_2O and the other set prepared with PO—underwent what we have dubbed environmental testing or high-temperature high humidity (HTHH) testing. The goal is to compare PO and H_2O samples in terms of their longevity and resistance to corrosion. The prepared samples (note that each sample is 7.6 cm by 2.6 cm BK7 float glass slide with a thickness of 1 mm and an RMS of < 1 nm) were placed in a circular sample holder inside a glass bell jar (Fig. 2). Two dummy glass slides (i.e., uncoated microscope slides) were inserted at the beginning and end of the sample lineup to ensure that all the samples experienced identical testing conditions. The intent is that the dummy

Fig. 2 Glass bell jar used in HTHH testing. Once prepped, the jar would be sealed with high-temperature vacuum grease and then be placed inside an oven.

glass slides allow the first and last samples in the lineup to feel the same environmental pressures as the slides in the middle of the lineup. At the start of a HTHH test cycle, 62 g of potassium chloride and 3.1 g of (5%) non-iodized sodium chloride were placed at the bottom of the jar. The jar was then sealed with high-temperature vacuum grease, placed in an oven set to 80°C, and allowed to sit until it had reached equilibrium with the oven. The oven had a sheet of aluminum foil covering the inside of the door to minimize heat loss through the door. Subsequently, 45 mL of distilled deionized water was injected into the salt mixture via a PTFE tube inserted into the jar which was then snapped off, sealing the jar for the remainder of the cycle. The concentration of salts dissolved in solution has been previously standardized by UCO to ensure that as long as a temperature of 80°C is maintained, then the jar will remain at 80% humidity for the duration of a single HTHH test cycle. The samples were left under these conditions for 19 h (i.e., a single HTHH test cycle corresponds to 19 h), after which the samples were removed from the jar. Subsequently, spectral reflectance was taken using a Cary 5000 UV-Vis-NIR spectrophotometer across the range of 200 to 3500 nm. Using the VW Absolute Specular Reflectance Accessory, the samples were measured with a beam width of less than 6.5 mm and had an incident angle of 7 deg. The samples were photographed with a Samsung SM-N986U—9 MP resolution—using a black velvet photography backdrop above the samples to reduce interference in photographing the sample's surface. The samples were then placed back into the jar to repeat the test cycle.

After the samples underwent a total of 10 cycles, spectroscopic ellipsometry was performed at an incident angle of 70 deg on the samples using the FilmTek 4000 (Scientific Computing International, Carlsbad, California, United States) spectroscopic reflectometry/ellipsometry system to collect the phase difference—Δ—and the complex ratio of p-polarized to s-polarized reflected light (r_p/r_s)—Ψ—of the samples between cycle 0 (i.e., a sample that did not undergo HTHH testing) and cycle 10.[14] In addition, using Q-Scope 250 Atomic Force Microscopy (AFM) with a Q-WM190 48 N/m tip, the cycle 0 samples and the samples after 10 cycles were imaged, with the resulting images interpreted using the Gwyddion data analysis software.[15] Moreover, due to its non-destructive nature and having a very limited number of samples to work with, scanning electron microscopy (SEM) and energy dispersive spectroscopy (EDS) were performed with data collected using acceleration voltage at 5, 7, 10, and 15 keV. All measurements, with the

exception of the whole-sample photographs, were done exclusively on the specular areas of the samples, as we intended to study how the original mirror surface evolved before obvious macroscopic signs of visible corrosion emerged. Therefore, data was not necessarily collected from the same area on the sample each time. With the exception of the AFM data, all the data was processed and graphed using GNU Octave.[16]

3 Results and Discussion

Figure 3 shows the spectral reflectance of the H_2O and PO samples prior to HTHH testing—$H_2O(0)$ and PO(0)—after eight HTHH test cycles—$H_2O(8)$ and PO(8)—and after 10 HTHH test cycles—$H_2O(10)$ and PO(10). The choice to include the eight HTHH test cycle spectral data was made as it more appropriately conveys how the PO samples held up in comparison to the H_2O samples. A notable feature of the PO(0) samples is their slightly higher reflectivity within the spectral range of 410 to 650 nm, which generally aligns with the absorption spectrum of hydrogen, suggesting that the H_2O samples contain a significantly higher level of hydrogen impurities. These impurities potentially contribute to a reduction in the overall spectral reflectance across the visible spectral range. This correlation underscores the potential impact of hydrogen-related absorption on the optical properties of the samples, indicating the necessity for careful consideration of such impurities in future analyses. Despite this observation, the spectra of $H_2O(0)$ and PO(0) are nearly identical, with the $H_2O(0)$ spectrum being lower than PO(0) by at most 1% across the range of 410 to 650 nm, with PO(0) having a percent reflectance of ~97.0% at 550 nm while $H_2O(0)$ was ~96.1% at 550 nm. After eight HTHH test cycles, the reflectance of $H_2O(8)$ significantly decreased to around 67.2% at 550 nm, whereas that of PO(8) showed considerable resilience by only degrading to around 84.3% at 550 nm over the spectral range that was investigated. In addition, PO(8) appears to degrade uniformly across the entire spectrum—retaining a consistent shape comparable to that of PO(0)—while $H_2O(8)$ degrades significantly more in both the ultraviolet and near-infrared ranges. Reaching 10 cycles, both PO(10) and $H_2O(10)$ appear fairly similar having gone beyond the point of catastrophic failure, suffering a significant reduction in spectral reflectance with $H_2O(10)$ falling to 56.9% and PO(10) down to 60.2% at 550 nm. This would indicate that over extended periods of long-term use, both PO and H_2O will be similarly degraded, but PO would be expected to have a longer operational lifetime as it degrades slower.

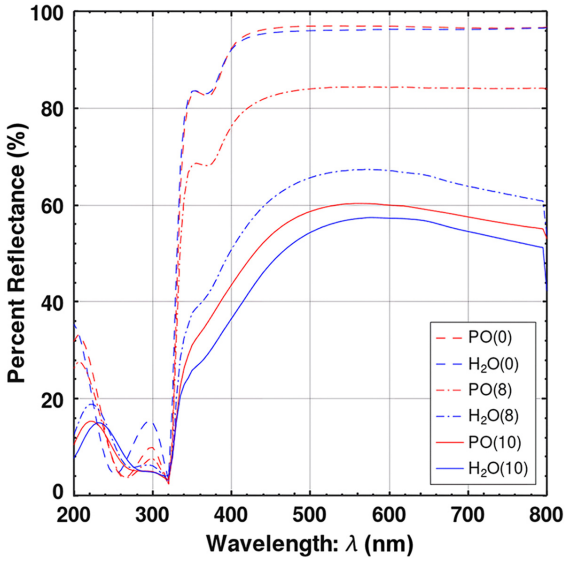

Fig. 3 Reflectance spectra of PO and H_2O samples: $H_2O(0)$ and PO(0), $H_2O(8)$ and PO(8), and $H_2O(10)$ and PO(10). There is little to no variation between $H_2O(0)$ and PO(0) and the variation present can easily be explained by minor inconsistencies with the evaporation process used to make the samples. After eight cycles, H_2O degraded down to under 70% reflectance at 550 nm while PO only fell to 84.3% reflectance. Having completed a full 10 cycles, both samples show significant degradation with spectral reflectance falling down to 56.9% for H_2O and 60.2% for PO.

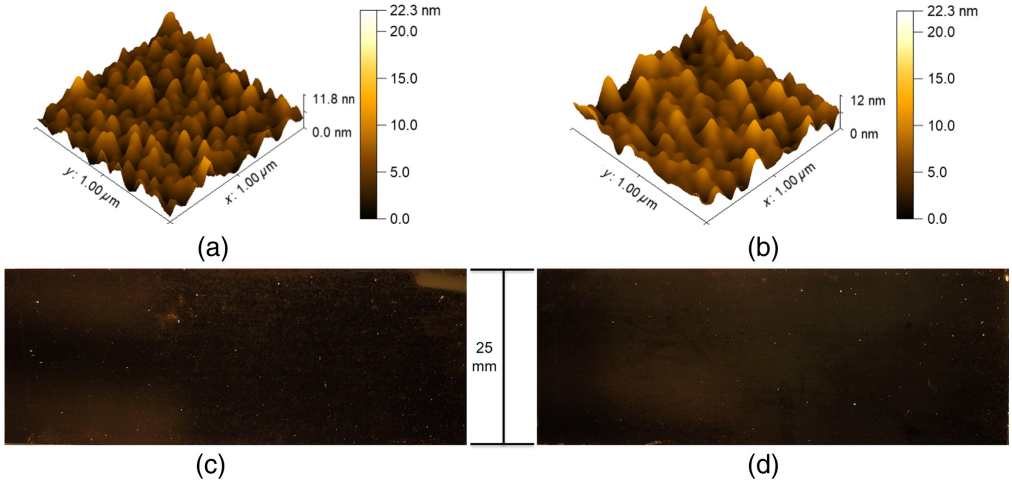

Fig. 4 (a) Surface morphology of $H_2O(0)$ with RMS roughness of 1.374 nm. (b) Surface morphology of PO(0) with RMS roughness of 1.491 nm. $H_2O(0)$ has a larger number of peaks with less variation in height while PO(0) has a larger variation in peak height. (c) and (d) Photos of the entire area of $H_2O(0)$ and PO(0), respectively, where smooth specular areas appear dark due to the black velvet photography backdrop.

Figure 4 shows surface morphology collected across a specular area by AFM and optical images of the whole sample area of $H_2O(0)$ and PO(0). $H_2O(0)$ in Fig. 4(a) shows general features characterized by a denser concentration of peaks and valleys while PO(0) in Fig. 4(b) shows lower density but a greater disparity between the peak heights, indicating that PO(0) is slightly rougher than $H_2O(0)$ as indicated by the RMS roughness; 1.491 and 1.374 nm for PO(0) and $H_2O(0)$, respectively. The respective optical images in Figs. 4(c) and 4(d) indicate both samples are similarly reflective and show no obvious differences, indicating the two types of samples were comparable prior to HTHH testing.

Figures 5(a) and 5(b) show surface morphology collected by AFM on $H_2O(10)$ and PO(10), respectively. Figures 5(c) and 5(d) show optical images of the whole samples of $H_2O(10)$ and PO(10), respectively, revealing that significant corrosion took place during the 10 HTHH test

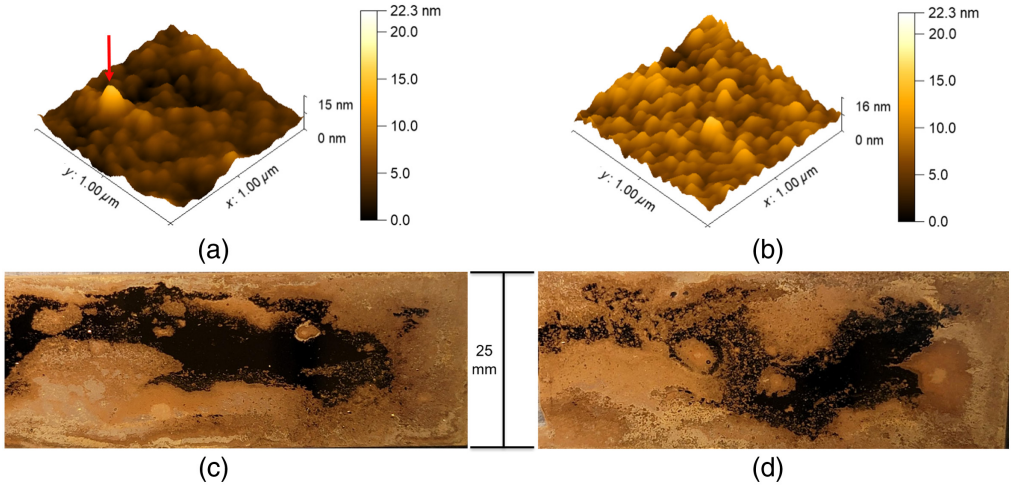

Fig. 5 (a) Surface morphology of $H_2O(10)$ with RMS roughness of 1.225 nm. (b) Surface morphology of PO(10) with RMS roughness of 1.383 nm. (c) and (d) Photos of the entire area of $H_2O(10)$ and PO(10), respectively, where specular areas appear darker in contrast to corroded areas which appear yellow to light brown. Both $H_2O(10)$ and PO(10) show a significant smoothing compared with $H_2O(0)$ and PO(0) shown in Fig. 4. $H_2O(10)$ underwent the most smoothing with all of the excess material appearing to have been pulled into distinctively tall peaks that appear as dots on the surface.

cycles. Corrosion began along the edges of the samples where the cross-section of a sample's layers is least protected by the AlO_x protective coating, which is in line with what we have observed in our previous works.[2–7] Similarly, a few point defect-induced pitting corrosion[17] formed during the first three HTHH cycles but did not significantly contribute to overall sample corrosion until cycles 8 or 9. Specular areas appear black while corroded areas appear to be a light yellow to orange in Figs. 5(c) and 5(d). RMS roughness reduced from 1.374 of $H_2O(0)$ to 1.225 nm of $H_2O(10)$ and from 1.491 of PO(0) to 1.383 nm of PO(10), indicating that the surface of both samples smoothed by 0.1 to 0.15 nm. PO(10) retained rather similar characteristics seen in Fig. 4(b) with the average peak height relative to the average valley depth decreasing by around 17% from PO(0) to PO(10). Conversely, on $H_2O(10)$ a small number of prime peaks —one of which is denoted by a red arrow in Fig. 5(a)—formed, seeming to have height in the range of 1.8 to 15 nm while heights of the surrounding satellite peaks have been significantly reduced in comparison to peaks in Fig. 4(a). A potential explanation is variation in peak height between $H_2O(0)$ and $H_2O(10)$ could reflect morphological non-uniformity between samples on the small scale that AFM operates. However, the total amount of material should be conserved (i.e., no material was explicitly added or removed from the samples during the HTHH testing) on the nominal surface of $H_2O(10)$, and the satellite peaks surrounding the prime peak have lost not only height but also their definition. As such, it would seem that an alternate plausible explanation is that $H_2O(10)$ underwent a type of Ostwald ripening whereby nearby material is pulled into the prime peak; such behavior is not unprecedented in metals.[18] In other words, material near a prime peak tends to diffuse preferentially into the prime peak, consequently compromising the AlO_x protective coating.

Comparing surface corrosion percentage across 0, 8, and 10 cycles for PO and H_2O, we found that from PO(0) to PO(8) nearly 59.1% of its surface could no longer be deemed specular as the surface suffered from corrosion damage. By contrast, $H_2O(0)$ to $H_2O(10)$ had 73.9% of its surface area no longer specular in appearance; this lines up well with the spectral reflectance data in Fig. 3. From PO(8) to PO(10), catastrophic failure occurs and the percentage of corrosion/damage on the surface rises 24.3% to a total of 83.4%. $H_2O(10)$ on the other hand, is already past its point of catastrophic failure and as such seems to degrade much slower from cycles 8 to 10. Despite more of PO(10)'s surface no longer being specular compared with that of $H_2O(10)$, Fig. 3 shows that PO(10) still maintains a more reflective surface.

The results of the SEM images, Figs. 6(a) and 6(b), of our samples after 10 cycles revealed significant pinhole damage associated with degradation of the AlO_x protective coating. Pinhole damage appears as black pixels in the SEM images, while all else represents a specular surface. $H_2O(10)$ in Fig. 6(a) shows pinholes up to 1.2 μm wide and an overall pinhole concentration of ~1.18% (i.e., the percentage of black pixels present in the SEM image). By contrast, PO in Fig. 6(b) shows pinholes smaller than 0.86 μm, with a much lower pinhole concentration of ~0.50%. Thus, indicating that further degradation of the samples is expected to continue more rapidly in the H_2O samples as they have more damaged areas across their protective coatings.

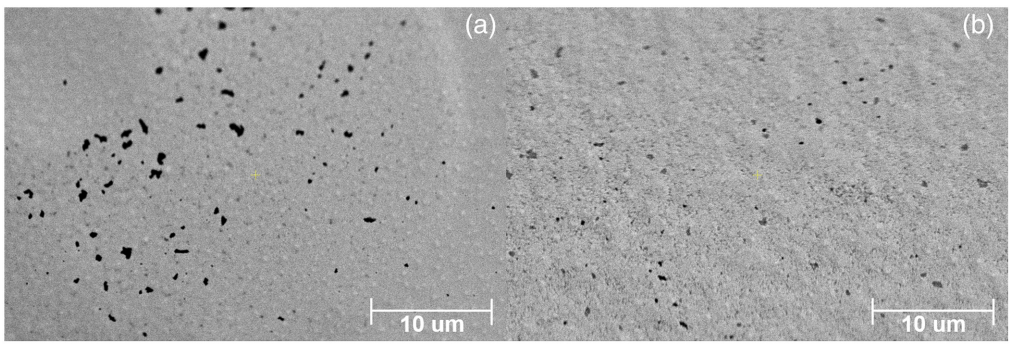

Fig. 6 SEM images of (a) $H_2O(10)$ and (b) PO(10) taken with a 5000× zoom. Black pixels represent areas of pinhole damage on the AlO_x protective coating. $H_2O(10)$ has large pinholes up to 1.2 μm in diameter while PO(10) has smaller pinholes below 0.86 μm.

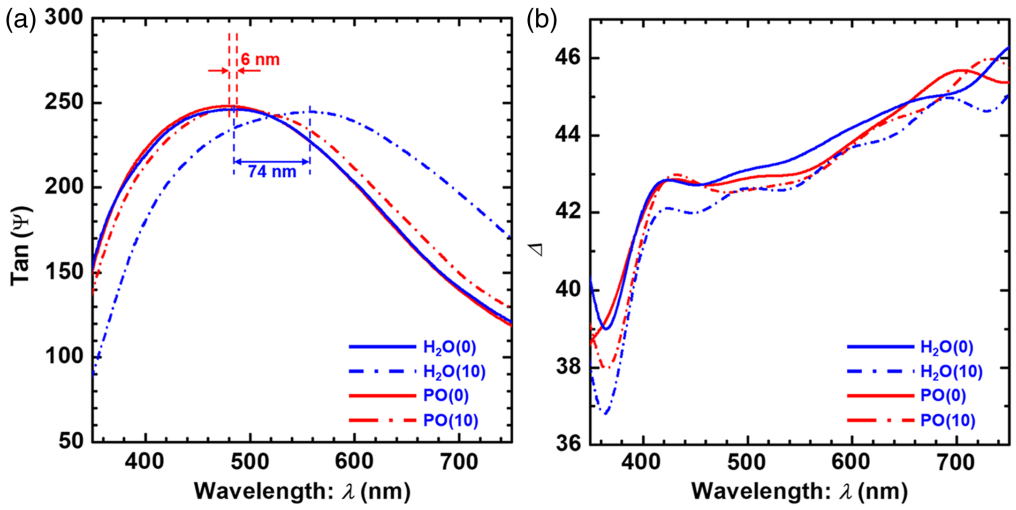

Fig. 7 Two quantities—Δ and Ψ—were obtained by ellipsometry performed within specular areas of the samples. The phase of the outgoing light—Δ—in H_2O samples shows a significant 74 nm redshift after 10 HTHH cycles while PO samples had a comparatively minimal 6 nm redshift. The change in the ratio of s to *p*-polarized light—Ψ—for both was minimal; however, the ratio of s to *p*-polarization change for H_2O was greater and more constant compared with PO where the ratio of *s* to *p*-polarization on average was similar before and after HTHH testing.

Figures 7(a) and 7(b) show phase Δ and Ψ, respectively, obtained by the spectroscopic ellipsometry performed on specular areas of the samples. Figure 7(a) reveals that $H_2O(10)$ underwent significant changes in terms of its surface structure, resulting in a 74-nm shift while PO(10) had a minimal shift of 6 nm, roughly only 8% to that of $H_2O(10)$. Figure 7(b) shows minimal changes in Ψ for both samples: a change at 550 nm by 0.73 deg for $H_2O(10)$ and by 0.15 deg for PO(10), indicating that the roughening of the surface has little impact on the relatives to *p*-polarization of the light. These changes in Δ and Ψ are attributed to surface evolution, as seen in Figs. 4 and 5, because local variations in film thickness and roughness are expected to significantly impact both Δ and Ψ.[14] The significant implication drawn from Figs. 4, 5, and 6 is that specular areas seem to have experienced significant microscopic transformations before reaching a catastrophic failure.

The EDS analysis was carried out as follows to obtain information on possible structural rearrangement that took place within the structure below the AlO_x protective coating. First, survey spectra were collected from areas that visibly appeared to be—panels (c) and (d) in Figs. 4 and 5—at various electron beam acceleration voltages. Because the interaction volume in which EDS signals (i.e., characteristic X-rays) are generated depends on the acceleration voltage, EDS signals collected at various acceleration voltages allow us to probe structural changes that occur at various material depths. Subsequently, peak intensity I_j of a chemical element j expected to be present in the samples was obtained from the survey spectra of $H_2O(0)$ and $H_2O(10)$ collected at a specific acceleration voltage V_A, providing I_j of $H_2O(0)$ and I_j of $H_2O(10)$ for V_A. The ratio —I_j of $H_2O(10)$ divided by I_j of $H_2O(0)$ at V_A—was obtained and plotted as a function of V_A in Fig. 8(a). The same procedure was used for PO(0) and PO(10) for Fig. 8(b). The penetration depths of the electron beam generated at various V_A were calculated using the Kanaya-Okayama expression (R_{KO}):

$$R_{KO} = 27.6AE_o^{1.67}/(\rho Z^{0.889}), \tag{1}$$

where A is the average atomic weight of a layer in grams per mol, E_o is the applied electron beam energy in kiloelectron volts, ρ is the density of a layer in grams per cubic-centimeter, and Z is the average atomic number of a layer.[19] The Kanaya-Okayama expression only reveals the maximum penetration depth. Thus, for multiple thin film structures for which the maximum penetration depth exceeds their total thickness, as in our case, the beam intensity needs to be reduced at the interface of the next layer relative to its reduction within the previous layer. As a result, the

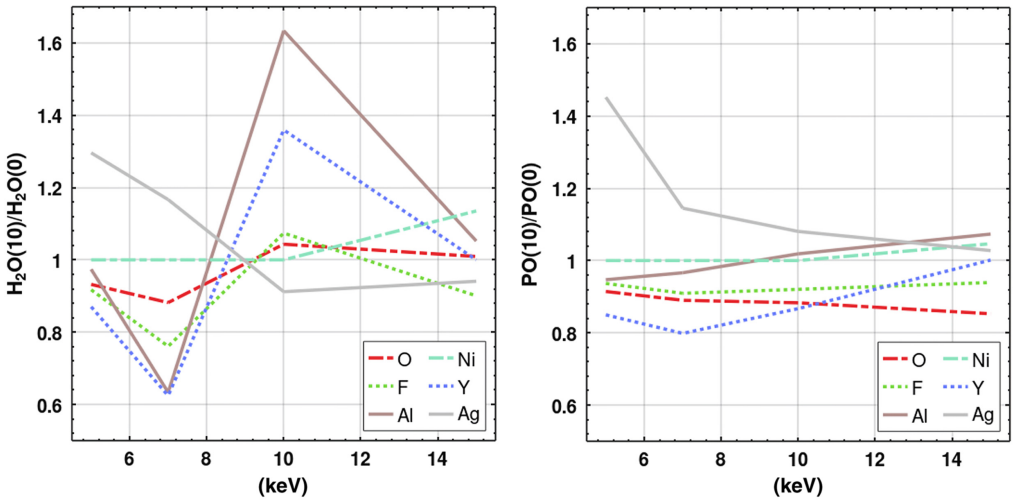

Fig. 8 EDS 10 cycle to 0 cycle ratio at varying electron accelerations (5, 7, 10, and 15 keV). H_2O is very unstable, while PO remains fairly consistent regardless of the depth of the scan.

range of V_A–5, 7, 10, and 15 keV—used in the experiment was found to correspond to a range of penetration depths of 250, 483, 1063, and 2341 nm, respectively. Because $H_2O(0)$ and PO(0) are expected to be identical, Fig. 8 qualitatively compares structural variations of $H_2O(10)$ and PO(10), directly revealing changes in the structural stability of the H_2O and PO samples over the HTHH testing. In other words, even in areas where apparent corrosion has yet to take place, local concentrations of constituent elements change correspondingly and are different from those that did not undergo HTHH testing. For example, in Fig. 8 for both H_2O and PO samples, Ag appears to have migrated closer to the samples' surface after 10 cycles of HTHH testing.

In Fig. 8, a ratio larger than 1 indicates an increase, in comparison to those in $H_2O(0)$ and PO(0), in the presence of a specific element for a given penetration depth or interaction volume. A comparison between Figs. 8(a) and 8(b) suggests that within the subsurface probed by the lowest V_A of 5 keV, both PO and H_2O samples show a general trend; a decrease in the ratio for all elements except Ag. As V_A increases probing deeper and increasing the interaction volume, the ratios for all the elements behave in ways substantially different in the two samples. As seen in Fig. 8(a), the $H_2O(10)$ shows a significant drop for all elements except Ag at 7 keV. As V_A further increases to 10 keV, all the elements except Ag increase while Ag drops below 1, and by 15 keV, the ratios of all the elements appear to be comparable to what they are at 5 keV. By contrast, PO(10) in Fig. 8(b) shows an elemental change that remains fairly stable once $V_A = 10$ keV is reached. There are a few notable features; however, Al appears to be reduced at the surface and increases monotonically as V_A increases. In addition, a large increase in Ag at $V_A = 5$ keV is seen, indicating that Ag in the Ag layer and Al in the AlO_x protective coating were able to freely trade positions during the HTHH environment testing. Interestingly, the amount of O and F in the sample appears to have decreased across the board, indicating that these elements were possibly given off as gasses during the HTHH testing. Similarly, Ag decreases as V_A increases, yet Ag remains above 1, seemingly indicating a net increase in Ag within the material, likely in part from the lateral increase in R_{KO} as well as a result of minor variation from the deposition process.

Figure 9 depicts the graph of the EDS ratio between $H_2O(0)$ and PO(0), revealing that there is generally a ± 0.2 variation in elemental concentrations between samples. On the surface of the samples, the EDS data indicates that H_2O samples have a higher Al-to-oxygen content compared to that of PO. Therefore, the improved corrosion resistance displayed by the PO samples could be attributed to having a higher oxygen-to-Al content. On the other hand, the higher Ag content could be attributed to pitting corrosion which would help to facilitate the Ag moving closer to the surface. The variation presented in Fig. 9 bolsters the idea that PO is highly stable/consistent between cycles 0 and 10 with most of the results falling within the ± 0.2 variance presented in the $H_2O(0)/PO(0)$ graph. Conversely, the EDS data further indicates how highly volatile the H_2O results are, falling upwards of 0.4 from unity between cycles 0 and 10.

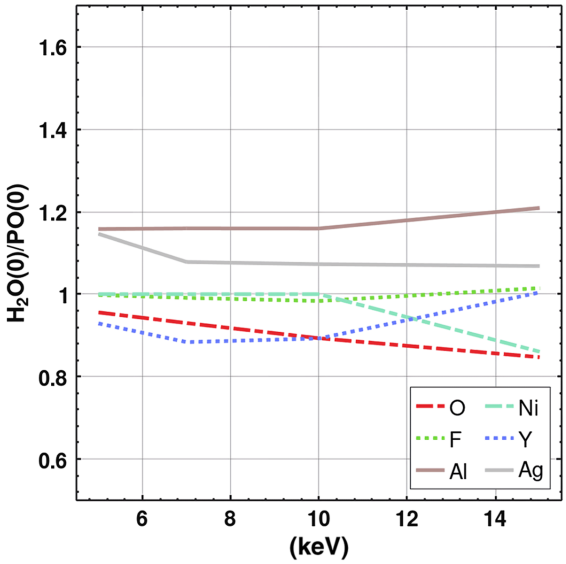

Fig. 9 EDS of $H_2O(0)$ to PO(0) ratio at varying electron accelerations (5, 7, 10, and 15 keV). With the exception of Ag and Al, the variation between samples on the surface is small. The variation present deeper in the structure is present between all the samples.

The migration of elements implied by Figs. 8(a) and 8(b) indicates that there is far less of a clear division between layers after the HTHH testing. This comes as no surprise as the samples were previously exposed to at most 60°C during the thermal ALD process. It seems quite likely that the 80°C environmental testing conditions were enough to allow for thermally driven internal reconstruction, which could have been further assisted by humidity-driven point defect pitting corrosion. Said pitting corrosion would pull metal atoms to the surface or even fully remove them from beneath the protective coating. The Ostwald ripening mentioned previously may be a variation of this material reconstruction in which metal atoms in the H_2O sample are pulled toward the surface, and the added thermal energy allows for the metal atoms to coalesce into a larger peak. In turn, as Fig. 9 implies that the ratio of Al to oxygen is different in the protective coating, then the H_2O samples could be more susceptible to damage, such as the pinhole damage seen in Figs. 6(a) and 6(b), from thermal cycling. That is to say, the multiple cycles of expansion and contraction as the samples heated and cooled could have induced fatigue in the H_2O AlO_x protective film. Internal material reconstruction may have worked in the favor of the PO sample, as the PO sample remained fairly consistent with minimal apparent changes to the remaining structure. As such, long-term use of mirrors covered with an AlO_x protection layer prepared with PO is expected to offer better endurance and provide a more consistent spectral reflectance compared with those covered with an AlO_x protection layer prepared with H_2O. This conclusion is further underscored especially when an AlO_x protection layer needs to be deposited at temperatures, such as 60°C, much lower than those normally used in AlO_x ALD processes.

4 Conclusion

Ag-based telescope mirrors require optically transparent protective coatings to function for extended periods of time without affecting the mirror's functionality. While AlO_x is one of the more viable options for a protective coating, how it is deposited has a significant impact on the ultimate lifespan of the mirror. The conventional method of using H_2O as an oxygen precursor works well for many applications; however, as our study clearly suggests, the use of PO (i.e., 80% ozone as opposed to the conventional 20%) would offer many benefits that H_2O is unable to do. For our specific objective—durable Ag-based mirrors, our study may lead to durable coatings that maintain the original optical performance for a much longer operating lifetime. When comparing between specular areas, PO had a minimal 6-nm phase shift compared with the 74-nm shift H_2O suffers from, indicating that over long-term use and despite appearing uncorroded, conventionally protected Ag mirrors will have significant variations in observational outcomes

even when looking at the same astronomical object. This conclusion is also supported by the EDS results that revealed the H_2O samples had rather erratic structural changes during the HTHH test cycles, while the PO samples maintained structural integrity. While not discussed directly in this paper, one factor potentially affecting the durability of the films is the density of the AlO_x protective coating. The expectation is that a pure ozone precursor should generate fewer pinholes during the deposition process and therefore a denser more robust film. It should be noted that the aforementioned pinholes are not related to similar breakdowns of the AlO_x protective coating that can occur as a result of Ostwald ripening and pit corrosion. As a part of our future investigation into PO films, we intend to examine the number of pinholes between H_2O and PO films as well as examine film densities. Further, we intend to investigate the structural changes in greater detail using secondary ion mass spectrometry (SIMS) and X-ray photoelectron spectroscopy (XPS) which may give us a clearer picture of elemental distribution and chemical characteristics across the surface of the samples. The said structural changes may result in the surface of the PO sample gradually degrading, as indicated by the relative consistency of the AFM data between the PO(0) and PO(10) samples, while the surface of the H_2O sample was compromised by the formation of tall peaks that absorbed surrounding material, fundamentally weakening the protective coating. Therefore, when deposited at 60°C as done in this study, the PO samples have conclusively proven to have significantly more durability leading to a 17% improvement in reflectance spectra in comparison to that of the H_2O sample.

Disclosures

The authors have no financial interests in the paper nor any other conflicts of interest to disclose.

Code and Data Availability

The raw/processed data required to reproduce these findings cannot be shared at this time as the data is part of an ongoing study.

Acknowledgments

This study was partially supported by Dr. John Hennessy at Jet Propulsion Laboratory, California Institute of Technology (Pasadena, California).

References

1. D. M. Fryauf, A. C. Phillips, and N. P. Kobayashi, "Annealing of high performance silver-based mirrors," *Proc. SPIE* **11800**, 1180008 (2021).
2. D. M. Fryauf, A. C. Phillips, and N. P. Kobayashi, "Critical processing temperature for high-performance protected silver mirrors," *J. Astron. Telesc. Instrum. Syst.* **7**(3), 034002 (2021).
3. F. Anjum et al., "Improving silver mirrors with aluminum oxynitride protection layers: variation in refractive index with controlled oxygen content by radiofrequency magnetron sputtering," *J. Astron. Telesc. Instrum. Syst.* **4**(4), 044004 (2018).
4. D. M. Fryauf et al., "Effect of intermediate layers on atomic layer deposition-aluminum oxide protected silver mirrors," *J. Astron. Telesc. Instrum. Syst.* **3**(3), 034001 (2017).
5. D. M. Fryauf, A. C. Phillips, and N. P. Kobayashi, "Corrosion protection of silver-based telescope mirrors using evaporated anti-oxidation overlayers and aluminum oxide films by atomic layer deposition," *Proc. SPIE* **9924**, 99240S (2016).
6. D. M. Fryauf, A. C. Phillips, and N. P. Kobayashi, "Corrosion barriers for silver-based telescope mirrors: comparative study of plasma-enhanced atomic layer deposition and reactive evaporation of aluminum oxide," *J. Astron. Telesc. Instrum. Syst.* **1**(4), 044002 (2015).
7. D. M. Fryauf, A. C. Phillips, and N. P. Kobayashi, "Moisture barrier and chemical corrosion protection of silver-based telescope mirrors using aluminum oxide films by plasma-enhanced atomic layer deposition," *Proc. SPIE* **8820**, 88200Y (2013).
8. R. W. Johnson, A. Hultqvist, and S. F. Bent, "A brief review of atomic layer deposition: from fundamentals to applications," *Mater. Today* **17** (5), 236–246 (2014).
9. Meiden America, "High-concentration/high-purity ozone gas generator: pure ozone generator," 2022, https://www.meidensha.com/catalog/MB64-3059.pdf.
10. Teledyne API, "OG-5000 series high purity ozone generator," 2017, www.teledyne-api.com/prod/Downloads/SAL000099C%20-%20OG-5000.pdf.

11. M. Kayanuma et al., "Theoretical study of the mechanism for the reaction of trimethylaluminum with ozone," *ACS Omega* **6**(40), 26282–26292 (2021).
12. Meiden Nanoprocess Innovations, Inc., "Evaluation of impurity gas in our pure ozone generator (MPOG-RDE01C)," NPG-200051-0, Unpublished internal company document (2021).
13. S. Jalili, F. Hajakbari, and A. Hojabri, "Effect of silver thickness on structural, optical and morphological properties of nanocrystalline Ag/NiO thin films," *J. Theor. Appl. Phys.* **12**, 15–22 (2018).
14. H. Fujiwara, Chap. 4 in *Principles of Spectroscopic Ellipsometry*, pp. 81–146, John Wiley & Sons Ltd, The Atrium, Southern Gate, Chichester, West Sussex (2007).
15. D. Nečas and P. Klapetek, "Gwyddion: an open-source software for SPM data analysis," *Cent. Eur. J. Phys.* **10**, 181–188 (2012).
16. J. W. Eaton et al., "Gnu octave, version 6.1.0," 2020, https://www.gnu.org/software/octave.
17. R. Srinivasan and F. Fasmin, An introduction to electrochemical impedance *spectroscopy*, 1st ed., Ch 6.4.2, CRC Press, Boca Raton (2021).
18. S. Wack et al., "Large-scale deposition and growth mechanism of silver nanoparticles by plasma-enhanced atomic layer deposition," *J. Phys. Chem. C*, **123**, 27196–27206 (2019).
19. J. I. Goldstein et al., *Electron Beam-Specimen Interactions*, pp. 53–122, Springer US, Boston, Massachusetts (1981).

Søren A. Tornøe is a graduate student working toward his PhD in electrical and computer engineering at the University of California Santa Cruz. He researches material science and thin film optics in the Nanostructured Energy Conversion Technology and Research Lab at UCSC. His areas of research include protective coatings for astronomical optics, green hydrogen from seawater electrolysis, and device electronics.

Brandon Cheney has been employed by the UCSC Department of Earth and Marine Sciences as an instrument engineer and material characterization specialist for just over 10 years. In his early career, he was employed as a failure analyst at Evans Analytical in Sunnyvale, CA, United States. He has been involved in the commercial agricultural process development for Taylor Farms in Salinas, CA, United States, and the aquaculture process development at the Natural Energy Labs in Kona, HI, United States.

Takayuki Hagiwara is employed at Meiden Nanoprocess Innovations, Inc., and is engaged in the development of deposition processes using pure ozone. He received his master's degree in 2014 from Gunma University.

Tetsuya Nishiguchi is a chief technology officer of Meiden Nanoprocess Innovations, Inc., and has been involved in the commercialization of a patented pure ozone technology that stores a large amount of distilled ozone and supplies nearly 100% of ozone gas to various semiconductor processes. He received his PhD in 2009 based on several papers clarifying the technical benefits of using the gas instead of commercially available low-concentration ozone gas and UV/plasma-enhanced oxidation technologies.

Nobuhiko P. Kobayashi joined UCSC in 2008, bringing extensive expertise in advanced electronic and photonic materials. At Hewlett-Packard Laboratories, he developed materials for memristive devices and nanowire photonics. At Lawrence Livermore National Laboratory, he studied semiconductor materials for high-speed diagnostics and optical CDMA. At Agilent Laboratories, he advanced LEDs, lasers, and transistors for fiber optics and wireless communications. He holds an MS and PhD degrees in material science from the University of Southern California, United States, earned in 1994 and 1998, respectively.

Biographies of the other authors are not available.